Final Draft
of the original manuscript:

Kashaev, N.; Ventzke, V.; Horstmann, M.; Chupakhin, S.; Riekehr, S.;
Falck, R.; Maawad, E.; Staron, P.; Schell, N.; Huber, N.:

Effects of laser shock peening on the microstructure and fatigue crack propagation behaviour of thin AA2024 specimens

In: International Journal of Fatigue (2017) Elsevier

DOI: 10.1016/j.ijfatigue.2017.01.042

Effects of Laser Shock Peening on the Microstructure and Fatigue Crack Propagation Behaviour of Thin AA2024 Specimens

Nikolai Kashaev, Volker Ventzke, Manfred Horstmann, Sergey Chupakhin, Stefan Riekehr, Rielson Falck, Emad Maawad, Peter Staron, Norbert Schell, Norbert Huber
Institute of Materials Research, Helmholtz-Zentrum Geesthacht,
Max-Planck-Str. 1, 21502 Geesthacht, Germany
nikolai.kashaev@hzg.de

Highlights

- Deep compressive residual stresses introduced without severe surface damages
- Significant FCP retardation observed due to compressive residual stresses
- LSP compressive residual stresses caused crack closure effect
- The crack closure effect increased opening load and reduced effective load range
- A methodology to consider the LSP residual stresses for the FCP behaviour proposed

Abstract
Laser shock peening (LSP) was performed on aluminium alloy AA2024 with a thickness of 2.0 mm. Microstructural studies using the electron back scatter diffraction (EBSD) technique were performed to quantify the micro-texture changes in the material through LSP. A residual stress analysis was performed using synchrotron radiation and a hole drilling technique. Fatigue crack propagation (FCP) tests were performed to investigate the retardation effect of LSP residual stresses. Load versus crack opening displacement curves were analysed to obtain the corrected values of load opening levels considering the effects of the residual stresses. Specimens with the LSP treatment reveal a significant retardation of the FCP. The presence of compressive residual stresses caused the crack closure effect, which increased the level of crack opening load and therefore reduced the effective load range. An original methodology to consider LSP-induced residual stresses on the FCP behaviour was proposed.

Keywords
LSP, AA2024, microstructure, EBSD, fatigue crack propagation, residual stress.
Paper type Research paper

1. Introduction

Laser shock peening (LSP) has been successfully used for extending the fatigue life of critical components. LSP imparts residual stresses that are considerably deeper than those of traditional methods, such as sand blasting or shot peening. Several researchers investigated LSP for retarding the growth of long fatigue cracks as well as effect of LSP on mechanical properties (Tan et al., 2004; Hatamleh et al., 2007; Hatamleh, 2009]; Hombergsmeier et al., 2014; Bergant et al. 2016). Tan et al. (2004) investigated the effects of LSP on the initiation and propagation of fatigue cracks in 2.5 mm-thick AA2024-T3 specimens with various notch geometries. The results clearly indicated that LSP is an effective surface treatment

technique for reducing or suppressing fatigue crack growth in aluminium alloys with various notch configurations.

Hatamleh et al. (2007) investigated the influence of LSP on the growth of fatigue cracks in friction-stir-welded sheets of 7075-T7351 aluminium alloy. The authors observed a significant decrease in the fatigue crack propagation (FCP) rates in specimens with LSP treatment versus those of untreated welds and base material (BM) specimens. The fatigue striation spacing for specimens with the LSP treatment was assessed and determined to be smaller compared to that in the BM specimens. The reduction in the striation spacing indicates a lower FCP rate and could be attributed to the deeper compressive residual stresses induced by the LSP.

Furthermore, a significant improvement in the FCP behaviour was demonstrated by Hombergsmeier et al. (2014) in the case of AA2024T3 M(T) specimens with two LSP-stripes outside the initial notch. The retardation effect of LSP on the FCP rate was attributed to high compressive residual stresses, which were generated in 2 mm-thick AA2024 sheets. Bergant et al. (2016) observed an inferior FCP behaviour of 10 mm-thick 6082-T651 C(T) specimens with LSP compared to that of BM specimens. The reason was probable in the un-optimised LSP process, which resulted in higher surface roughness without introducing noticeable compressive residual stresses in the investigated material.

There are a few studies that investigate the fatigue crack retardation mechanisms acting on a material with LSP residual stresses. Lados and Apelian (2006) published a comprehensive study on how to quantify and consider the effects of residual stresses generated through different heat treatments in Al-Si-Mg cast alloys on the FCP behaviour. The authors described mathematical techniques to consider residual-stress effects on the FCP rate data along with methods for eliminating residual stresses in specimens for the FCP test. Additionally, they reported mechanisms involved in the FCP through residual stress fields. The goal of the current study is to understand the effects of LSP residual stresses on the FCP behaviour of the commonly used aircraft aluminium alloy AA2024 with T351 heat treatment condition. This alloy is generally used in aircraft applications requiring high strength to weight ratios as well as good fatigue resistance. The primary focus was investigating the retardation mechanisms of LSP-induced residual stresses on the FCP.

2. Experimental methods

2.1. Materials and LSP trials

A 2.0 mm-thick aluminium alloy 2024 sheet with T351 heat treatment condition without a clad layer was used in this study. The investigated material has an engineering ultimate tensile strength of 490 MPa, yield strength of 370 MPa, and elongation to fracture of 16%. The Vickers hardness of the material is approximately 150 HV 0.2 (Enz et al., 2015 [3]).

LSP was conducted using a Q-switched Nd:YAG laser operating at 10 Hz with a wave length of 1064 nm and a pulse duration of 10 ns. A diffractive optic was used to deliver 3 J in a square spot of 3 mm x 3 mm on a specimen surface covered with an aluminium foil. The LSP was applied on the surface of C(T) specimens with an initial crack length a_0 = 10 mm. The treated specimen area was 15 mm x 15 mm. The sequence of LSP spots is depicted in Figure 1(a). Numbers of overlapping LSP treatment indicate how many times LSP was applied at

the same location: 1 time (1x, no overlapping), 3 times (3x overlapping) and 5 times (5x overlapping). The LSP treatment was applied on both sides of each C(T) specimen. The distance before the area of the LSP patterns and the initial crack tip was 1 mm for the two specimens LSP 1x -1 and LSP 5x -1, and 2 mm for the two specimens LSP 3x -2 and LSP 5x -2. The specimens investigated in this study are summarised in Table 1.

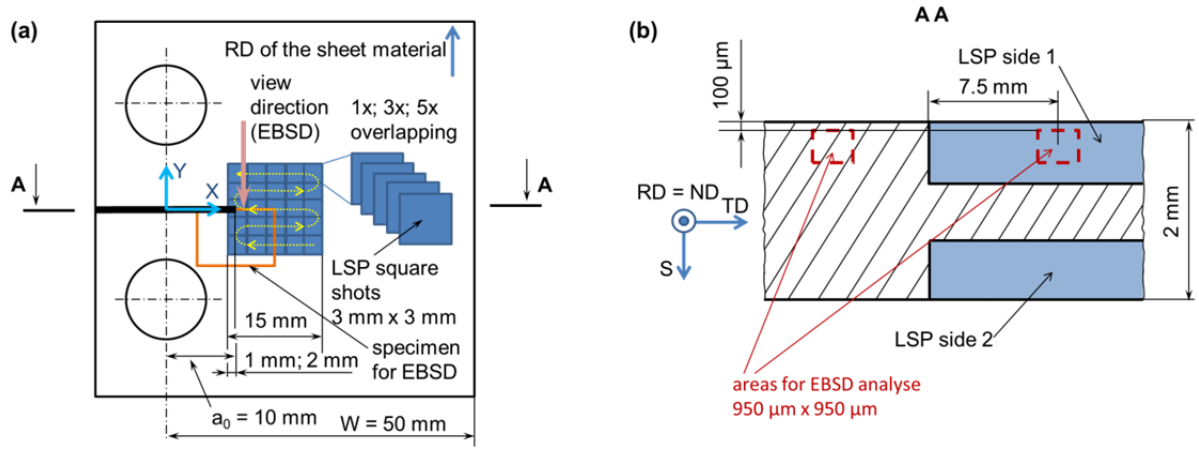

Figure 1. *Geometry of the specimens.*
(a) Positioning of the LSP patterns on the C(T) specimen; and (b) positioning of the areas for the EBSD analysis;
"RD", "TD" and "S" denote the rolling direction, transverse direction and thickness direction of the sheet material, respectively. The normal direction (ND) is parallel to the RD of the sheet.

Table I. *Specimen documentation*

Specimen identification	Numbers of LSP overlapping areas	Distance of LSP patterns before the crack tip
BM	-	-
LSP 1x -1	no overlapping	1 mm
LSP 5x -1	5	1 mm
LSP 3x -2	3	2 mm
LSP 5x -2	5	2 mm

2.2. Microstructural characterisation

The microstructure of the BM specimens and the LSP treated specimens was studied using SEM with electron back-scatter diffraction (EBSD). The EBSD measurements were performed in the near surface region, where the distance from the specimen surface to the upper corner of the analysed area of 950 µm x 950 µm was approximately 100 µm. The specimen for the EBSD analysis was extracted from the middle LSP area (Figure 1(b)). The specimen was analysed at 30 kV, beam current of 0.3 nA, emission current of 75 µA, magnification of 100x, working distance of 13 mm, step size of 2 µm, and sample tilt of 70°. The orientation calculation was based on the generalized spherical harmonic expansion (GSHE) method and assumed a triclinic sample symmetry. In inverse pole figures, the rolling direction (RD) is

[001]. The microhardness profiles in the cross-sections of the metallographically prepared specimens were obtained using an automated Vickers hardness testing machine.

2.3. Residual stress analysis

The determination of the residual stresses was performed at the P07B station of the HZG beamline HEMS (High Energy Materials Science), which was located in the PETRA III synchrotron radiation source at DESY (Deutsches Elektronen-Synchroton, Germany). The transverse residual stresses σ_{xx} and longitudinal residual stresses σ_{yy} (Figure 1(a)) were determined in a transmission setup using a photon energy of 87.1 keV (wavelength of 0.1429 Å) as well as a beam with a cross-section of 0.5 mm × 0.5 mm. A Perkin-Elmer area detector with a pixel size of 200 µm at a distance of 1448 mm from the specimen was used for recording complete diffraction rings. A specimen area of 30 mm × 45 mm was covered with 30 scan lines of 45 points each, thus resulting in a point mesh with 1 mm distance between the points and 1426 points (specimen LSP 5x -2). Only a smaller area of 15 mm × 45 mm was covered for sample LSP 3x -2. Data reduction was performed using the program Fit2d (Hammersley et al., 1996). The scattering angle 2Θ of the Al (311) reflection was determined by fitting a Gaussian profile to the measured peaks. Strains were calculated from the shifts in the peak position. The stress-free lattice parameter was determined from the balance of forces along a line from the notch to the opposite specimen edge; the integral of σ_{yy} along that line must be zero. The residual stresses were calculated from the strains using a Young's modulus of E = 69.4 GPa and a Poisson's ratio ν = 0.35 for the (311)-reflection. For details on the residual stress analysis using diffraction, refer to the book of Lodini and Fitzpatrick (2003).

To determine the depth-resolved residual stresses, the hole drilling equipment "Prism" was used. "Prism" is equipped with an optical electronic speckle pattern interferometer (ESPI) system that provides high-quality full-field data for accurate residual stress determination. This technique has been described in detail by Steinzig and Ponslet (2003).

2.4. Fatigue crack propagation test

The specimens used for the FCP test are compact tension (C(T)) specimens based on the ASTM E647-11 standard with a width W = 50 mm. All C(T) specimens were machined with the loading axis parallel to the rolling direction of the sheet material. An initial crack a_0 = 10 mm was introduced by an electro discharge machining. The stress intensity factor range, ΔK, can be calculated based on the mentioned standard as follows:

$$\Delta K = \frac{\Delta F}{B\sqrt{W}} \frac{\left(2+\frac{a}{W}\right)\left(0.886+4.64\frac{a}{W}-13.32\left(\frac{a}{W}\right)^2+14.72\left(\frac{a}{W}\right)^3-5.6\left(\frac{a}{W}\right)^4\right)}{\left(1-\frac{a}{W}\right)^{1.5}}, \quad (1)$$

where a, B and ΔF are the crack length, specimen thickness (2 mm) and load alternation, respectively.

The FCP tests were conducted using a servo-hydraulic machine with a capacity of 25 kN. Each specimen set was submitted to the same test conditions, i.e., a load ratio, $R_F = F_{min}/F_{max}$ of 0.1, frequency of 10 Hz and room temperature. All specimens were polished in the area where the crack expected. The fatigue cracks were monitored on the surface using the

optical microscope. The crack growth was curved automatically using a clip in the crack mouth, and a second measurement consisted of periodic measurements of the locations of the crack tip using an optical microscope. For both methods, the crack growth was curved using the crack length data as a function of the number of cycles. For example, the incremental polynomial method involves fitting a sixth-order polynomial to sets of data points. The method allows the data to be filtered to reduce the margin of error. The crack opening displacement (COD) clip was mounted on the top side of each C(T) specimen before the FCP test. During the FCP test, the applied load vs. COD curves were obtained.

3. Results

3.1. Microstructure and residual stress

Figure 2 depicts the crystal orientation maps and the corresponding [001] inverse pole figures obtained in the edge region of the AA2024 BM (Figure 2(a) and (b)) and the area influenced by LSP (Figure 2(c) and (d)). The different colours in the crystal orientation maps (Figure 2(a) and (c)) indicate different crystal orientations parallel to the normal direction (ND=[001]). The AA2024 BM depicts grains elongated through the rolling process with an average grain size of 36.6 µm ± 18.8 µm. From the inverse pole figure (Figure 2(b)), it can be observed that the maximum axial intensity (H_{max} = 1.75 mrd) exists at the crystal orientation <1 1 2> // ND with an spread angle of approximately ±15°. Furthermore, the maximum transverse in an orientation band occurs in the crystal direction <0 1 2> // ND with an spread angle of approximately ±5° (H = 1.18 mrd). Compared to the BM, the area influenced by the LSP depicts axial intensities from 1.74 mrd to 1.93 mrd for the <1 1 2>//ND and 1.18 mrd to 1.06 mrd for the <0 1 2>//ND (Figure 2(d)).

The confidence index (*CI*) provides a measure of the quality of the EBSD measurement. For the AA2024 BM, *CI* = 0.55 indicates the appropriate quality of the EBSD measurement and is comparable to *CI* = 0.54 of the LSP-influenced area. The differences were obtained in the image quality (*IQ*) values, i.e., *IQ* = 3131.61 for the BM and *IQ* = 2810.84 for the LSP-influenced area. The *IQ* value is determined using the contrast and brightness of a Kikuchi diffraction image. The Kikuchi diffraction image is used for the identification of the crystal plane (hkl) and determination of the Euler angles (φ_1, φ_2, φ_3), which is affected by the density of the defects. The high density of defects reduces the brightness and contrast of the Kikuchi diffraction image and thus the *IQ*-value. Therefore, the lower *IQ*-value for the LSP influenced area indicates that through the LSP treatment, the density of defects increased. However, morphological changes of microstructure regarding grain shapes were not observed in the LSP-influenced area.

The recalculated (1 1 1) and (1 1 0) pole figures of the BM and the LSP-influenced area indicate the presence of a nearly orthorhombic symmetry of the specimens (Figure 3). The position of the pole densities in both the BM and LSP-influenced areas is nearly identical, where the distribution of the orientation bands and pole density is different. The obtained maximum pole densities for the BM (P_{max} = 2.013 mrd) and LSP-influenced areas (P_{max} = 2.171 mrd) indicate a relatively weak microtexture due to the presence of a high number of different crystal orientations. The pole density in the S-direction of the (1 1 1) pole figure obtained from the LSP-influenced area is higher than that of the corresponding BM.

Therefore, it can be assumed that the interaction between the laser-induced shock waves primarily interacted with crystals in the <1 1 1>//S crystal direction.

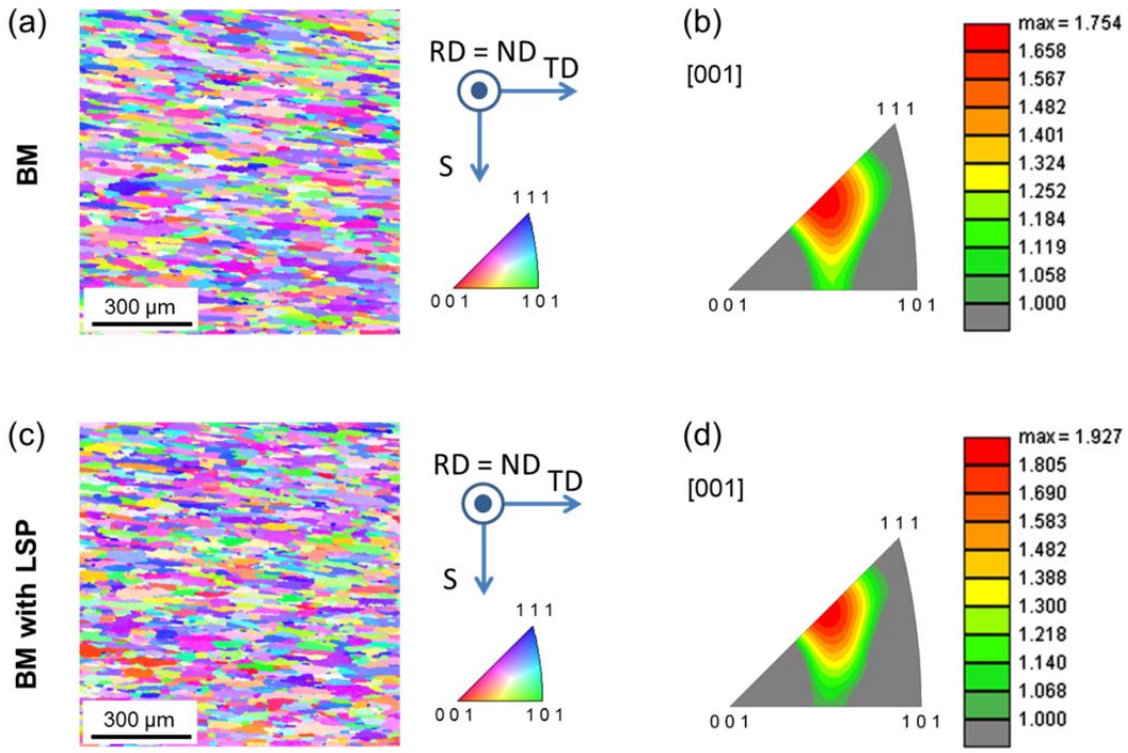

Figure 2. *Crystal orientation maps and inverse pole figures obtained from the sub-surface regions of the BM and the LSP treated specimen.*
(a, b) BM (H_{max} = 1.754 mrd, L = 22, ω = 5°) and (c, d) LSP treated specimen (H_{max} = 1.927 mrd, L = 22, ω = 5°). The distance from the surface to the upper corner of the maps was approximately 100 µm. ("RD", "TD" and "S" denote the rolling direction, transverse direction and thickness direction, respectively, of the sheet material. The normal direction (ND) is parallel to the RD of the sheet. The LSP treatment was applied with 5x overlapping.

A quantitative EBSD analysis was performed. Details regarding the area-related fractions of the crystal directions are provided in Table 2. It can be clearly seen that all of the represented crystal directions <u v w>//ND vary throughout the LSP process. The crystallites with crystal directions <1 1 2>//ND and <0 1 2>//ND depict the most significant changes in their increased area-related fraction. Furthermore, the area-related fractions of other crystallite directions decreased.

It can be concluded from the EBSD analysis that the microstructural changes due to local LSP treatment are relatively moderate compared to those obtained in the study by Gariépy et al. (2013). Gariépy et al. (2013) investigated the microstructural state of AA2024-T351 after it was shot peened using the EBSD analysis. The authors observed an unindexable structure in the first few micrometres with large dislocation densities and extremely small dislocation substructures. They measured significant lattice rotations over distances of approximately 100 µm up to a depth of 70 µm. Contrary to shot peening, the applied LSP treatment in the current study does not depict this type of microstructural damage in the sub-surface region of the LSP areas. Thus, the LSP is an extremely promising process for the generation of compressive residual stresses without noticeably damaging the specimen surface region. In

this study, the selected process parameters for the LSP treatment of AA2024-T3 were suitable to avoid surface damages as well as deformations in the microstructure.

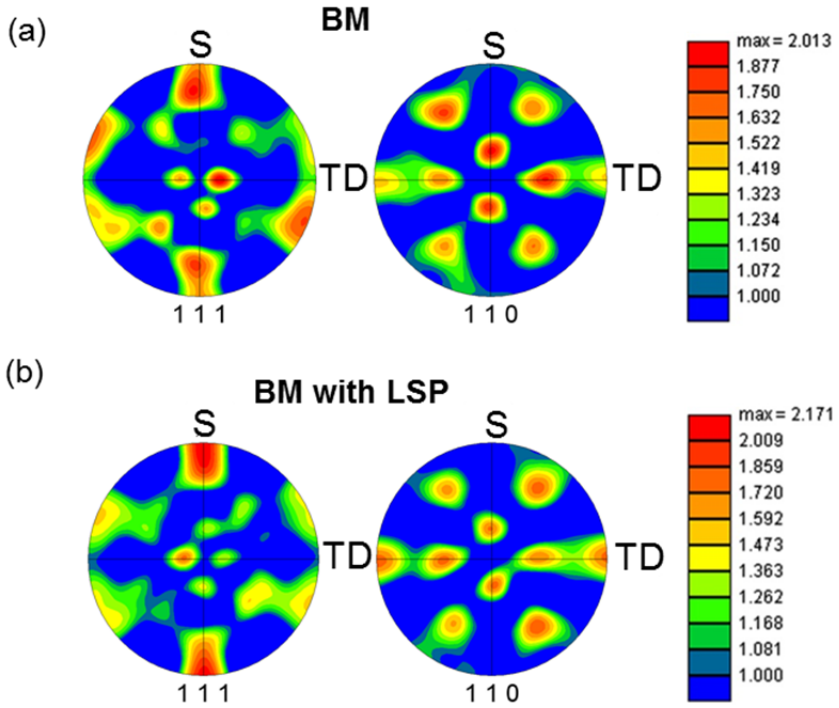

Figure 3. Typical (1 1 1) and (1 1 0) pole figures of the sub-surface regions of (a) BM; and (b) LSP treated specimen.

(a) BM (P_{max} = 2.013 mrd, L = 16, ω = 10°) and (b) BM with LSP (P_{max} = 2.171 mrd, L = 16, ω = 10°). The distance from the surface to the upper corner of the maps was approximately 100 µm. ("TD" and "S" denote the transverse direction and the thickness direction, respectively, of the sheet material (Figure 1(b)). The LSP treatment was applied with 5x overlapping.

The results of the residual stress analysis (RSA) using synchrotron radiation are illustrated in Figure 4. It should be noted that the diffraction-based RSA in the transmission setup yields the stresses integrated over the sample thickness. The calculated full width at half maximum (FWHM) maps for the two specimens with LSP treatment indicate a relatively low LSP-induced plasticity in the area of the LSP treatment (indicated by the dashed square) (Figures 4(a) and (b)). It is in good accordance with the EBSD results mentioned above, which indicated only rotation of the crystals without any deformation. The low work-hardening is a typical property of the LSP process based on the process conditions and parameters adjusted to AA2024-T351, as indicated in this study. Rouleau et al. (2011) emphasised that the first interesting result is the negligible work-hardening and plastic deformation effects after the LSP treatment of the Al-Cu-Li alloy AA2050-T8.

Table 2. *Area-related fractions of the crystals directions in the BM and LSP-influenced areas*

Number	<uvw>//ND	Fraction BM [%]	Fraction LSP [%]
1	<1 1 2>//ND	6.7	15.8
2	<2 2 5>//ND	4.7	3.3
3	<0 6 11>//ND	7.2	7.6
4	<0 1 2>//ND	3.8	7.6
5	<0 3 7>//ND	8.5	7.5
6	<6 3 4>//ND	16.9	15.6
7	<2 1 3>//ND	17.4	15.0
8	<2 1 5>//ND	14.6	12.3
9	<6 3 2>//ND	12.8	10.2
10	<8 4 3>//ND	7.3	5.0

The data obtained are based on the inverse pole figures presented in Figures 2(b) and (d)

The measured residual stress maps are illustrated in Figures 4(c)-(f). Close to the crack tip, tensile residual stresses through the thickness are present. In the range of a/W values of approximately 0.27 to 0.48, compressive residual stresses through the thickness are present. The values of the compressive residual stresses and sizes of the areas with compressive residual stresses are nearly comparable between the two specimens with the LSP treatment (LSP 3x -2, Figures 4(c) and (e), and LSP 5x -2, Figures 4(d) and (f)). The compressive residual stresses through the thickness are compensated with tensile residual stresses through the thickness, which have the highest values at the boundaries of the LSP treated areas. The tensile residual stresses through the thickness in the *x*-direction, σ_{xx}, depict the highest values at the LSP boundaries in the *y*-direction (y = -7.5 mm and y = 7.5 mm, Figures 4(c) and (d). In contrast to σ_{xx}, the tensile residual stresses through the thickness in the *y*-direction, σ_{yy}, depict their highest values at the LSP boundary in the horizontal (crack propagation) direction (a/W = 0.5, Figures 4(e) and (f)).

Figure 5 illustrates the residual stress measurement results obtained using the hole drilling technique. The measurements were performed at 3 locations in the middle of the LSP area from both sides of the specimen. Using a tool diameter of 2.0 mm, it was possible to obtain the residual stress profiles up to a half specimen depth (1 mm). The results obtained from both sides are provided in Figure 5. The BM specimen depicts a non-uniform depth-resolved residual stress profile, where the residual stresses σ_{yy} are slightly higher than the residual stresses in the *x*-direction, σ_{xx}. The surface regions depict tensile stresses, which are compensated through the compressive residual stresses in the core region of the BM. This residual stress state can be caused by the rolling process of the sheet material.

The LSP treated specimen indicates the highest compressive residual stress at depths of approximately 0.2 mm (LSP side 1) and 0.1 mm (from the specimen surface, depth value 1.9 in Figure 5, LSP side 2). The compressive residual stresses, σ_{yy}, are significantly higher than the compressive residual stresses σ_{xx}. It should be noted that the values obtained of the compressive residual stresses of approximately 450 MPa are higher than the yield strength of the material investigated (370 MPa). Because the hole drilling technique overestimates the residual stress values when they are close to the yield strength of the material, as

investigated by Chupakhin et al. (2015), the actual residual stress values should be lower. Nevertheless, the hole drilling technique provides a useable qualitative result. It can be seen that even in the centre of the specimen, the compressive residual stresses occur in both directions. The results indicate that by using the LSP treatment, the generation of compressive residual stresses through the thickness is possible.

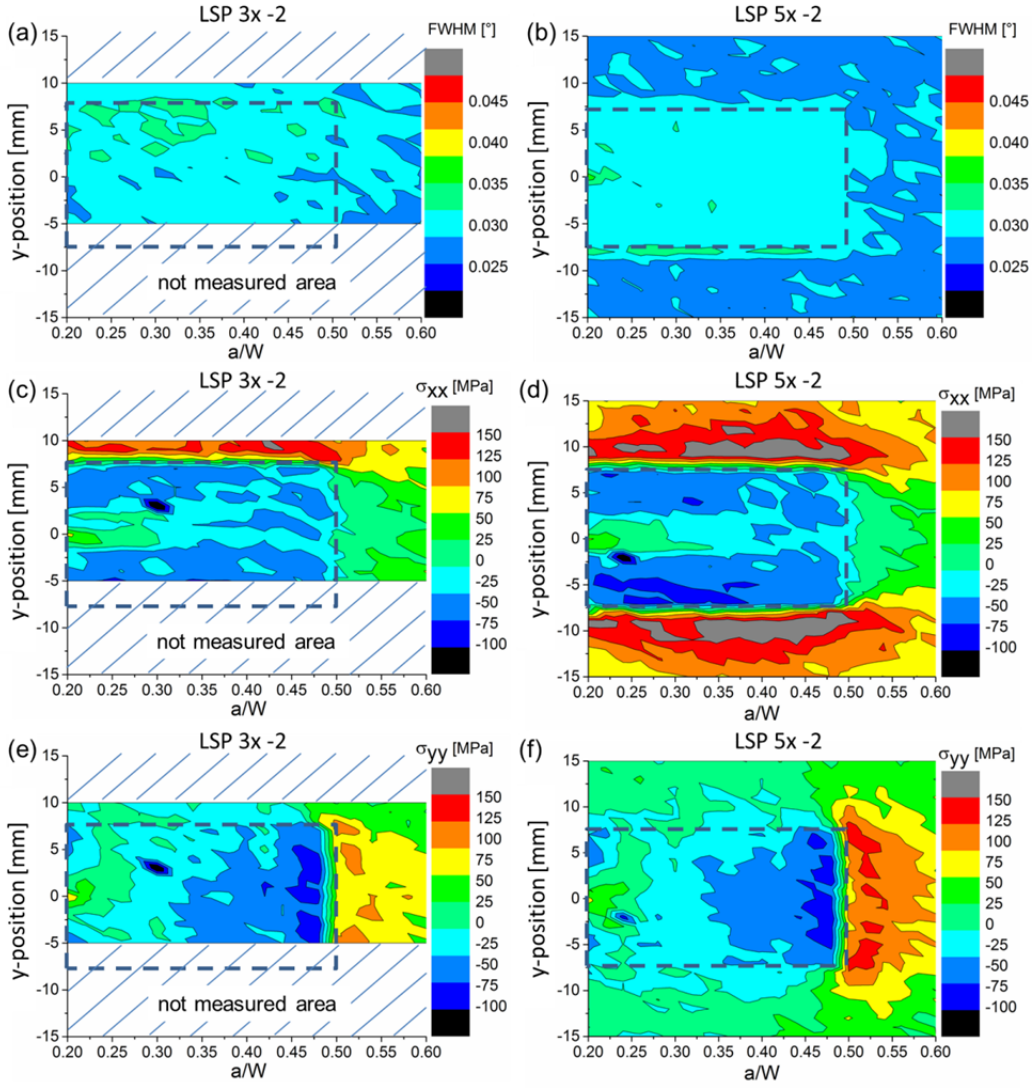

Figure 4. *FWHM and RS maps for 2 specimens with LSP treatment.*
(a), (c) and (e) obtained for specimen LSP 3x -2 (3x overlapping); and (b), (d) and (f) obtained for specimen LSP 5x -2 (5x overlapping)

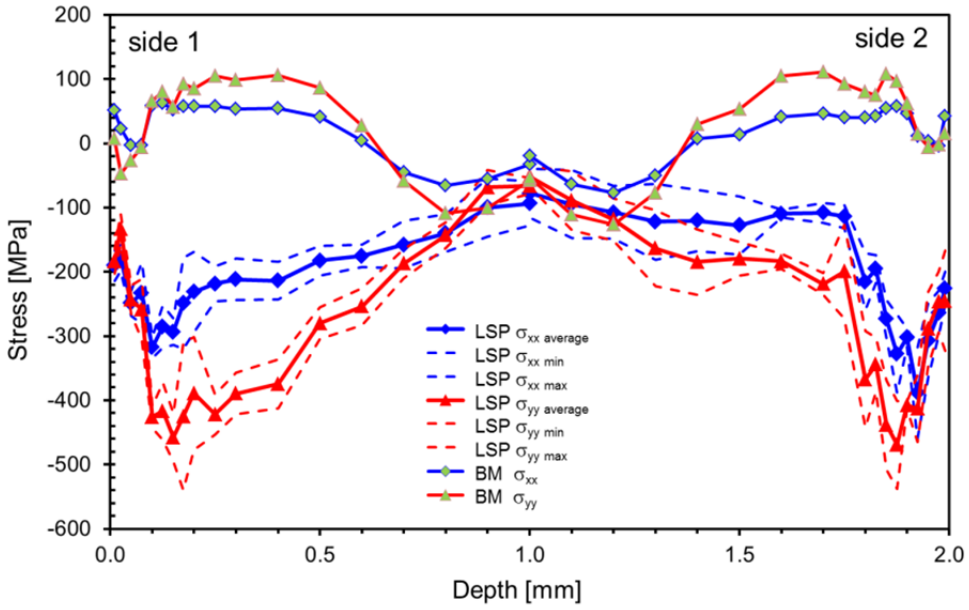

Figure 5. *Residual stress profile measured using the hole drilling method for the C(T) BM specimen and the specimen with LSP (5x overlapping) at three points in the middle of the LSP-area with an average curve from both sides of the specimen.*

The results of the microhardness measurements are depicted in Figure 6. The microhardness profiles were obtained through the sheet thickness of a BM specimen and a LSP treated specimen. The results indicate that a slight microhardness increase occurs from approximately 150 HV 0.1 (mean microhardness of the BM) in the surface regions of the LSP treated specimen to a microhardness-value of approximately 175 HV 0.1. The microhardness profile of the LSP treated specimen can be correlated with the residual stress profiles illustrated in Figure 5. For the measured residual stress profiles, the effects of the LSP are more pronounced on side 1 (1st side for the LSP treatment), where the maximum compressive residual stress, σ_{yy}, is at a depth of approximately 0.2 mm (from the specimen surface). The maximum compressive residual stress, σ_{yy}, on side 2 is located at a depth of approximately 0.1 mm (from the specimen surface, at a depth value of approximately 1.9 in the diagram). The results of the microhardness measurements indicate the same trend as the residual stress measurement results, in which a slight increase in the microhardness is more pronounced on side 1 (Figure 5). The increase in the microhardness by around 5% in areas with highest compressive residual stress is in good agreement with the model proposed by Huber and Heerens (2008), assuming that only the uniaxial compressive residual stresses σ_{xx} remains present in the cross-sectioned and indented surface. Because the increase in microhardness can be fully attributed to the effect of residual stress, possible contributions from work hardening due to the LSP treatment are insignificant.

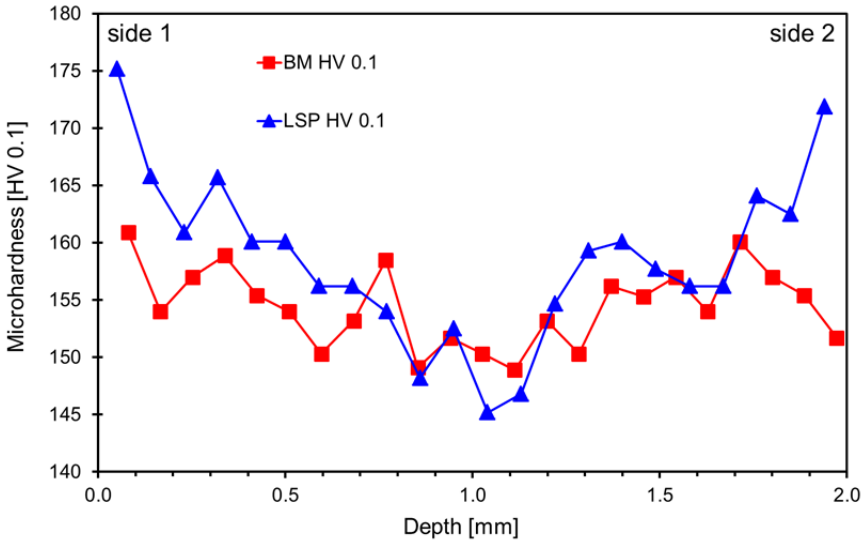

Figure 6. *Microhardness profiles of the BM specimen and the LSP treated specimen (LSP 5x -1).*

3.2. Fatigue crack propagation

Figure 7 depicts the FCP test results. The FCP behaviour of the LSP treated specimen LSP 1x -1 (no overlapping) is close to the FCP behaviour of the BM specimen and indicates that the LSP treatment did not generate significant compressive residual stresses in the C(T) specimen. This indicates that the effect of LSP process with the laser energy of 3 J and the square spot size of 3 mm x 3 mm on the FCP behaviour is not significant if only one layer of LSP treatment (no overlapping) is applied. Therefore, for further investigations only LSP treated specimens with 3x and 5x overlapping were considered.

The LSP treated specimens (3x and 5x overlapping) depict a significantly higher number of cycles required for propagating the fatigue crack to an *a/W* value of 0.6 (crack length, *a*, divided by the C(T) specimen width from the pin holes, *W* (50 mm), Figure 7(a)). At the beginning of the FCP test up to approximately 47,000 cycles, specimens LSP 3x -2 and LSP 5x -1 indicate slightly higher values of *a/W*. This result can be explained due to the presence of tensile residual stresses through the thickness at the front of the crack tip, which are depicted in Figure 4(e) for specimen LSP 3x-2. The fatigue life of the LSP treated specimens with 5x overlapping increased by a factor of nearly 3.5 compared to the BM specimen. The FCP rate, *da/dN* vs. *a/W*, as indicated in Figure 7(b), demonstrates a significant retardation in the FCP when the crack propagates through the LSP treated area with high compressive residual stresses through the thickness. The retardation of the FCP rate is more significant for specimens with the LSP treatment and 5x overlapping (LSP 5x -1 and LSP 5x -2). At an *a/W* value of approximately 0.5 (border of the LSP area), where tensile residual stresses through the thickness occur, the FCP rate increases with an increasing *a/W*. At an *a/W* value of approximately 0.6, the FCP rates of LSP treated specimens reach the FCP rate of the BM specimen.

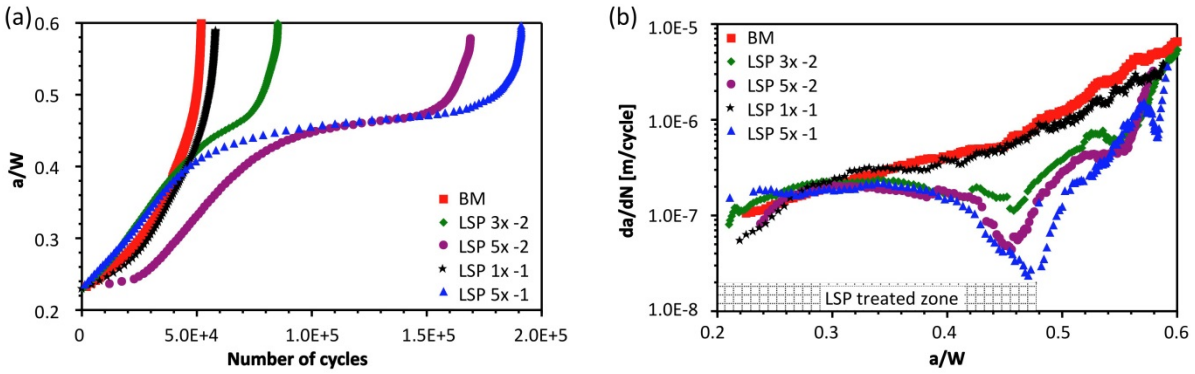

Figure 7. *FCP test results.*
(a) a/W vs. number of cycles; and (b) da/dN vs. a/W.

3.3. Fatigue crack trajectory and fractography of fractured surfaces

Fatigue crack propagation trajectories were determined on side faces of C(T) specimens. On a macroscopic scale, the fatigue crack of the BM specimen (Figure 8(a)) started from the initial notch and propagated slightly downwards, and then from a crack length of approximately 18 mm to the end of the test the fatigue crack propagated almost horizontally. In comparison to the BM specimen the crack path of the LSP treated specimen (Figure 8(b)) is characterized by essentially more pronounced variations in FCP direction within the LSP treated area. Furthermore, the distance between the crack flanks is smaller than in the BM specimen. Therefore it can be assumed, that residual stress condition in LSP treated specimen has decreased the crack opening.

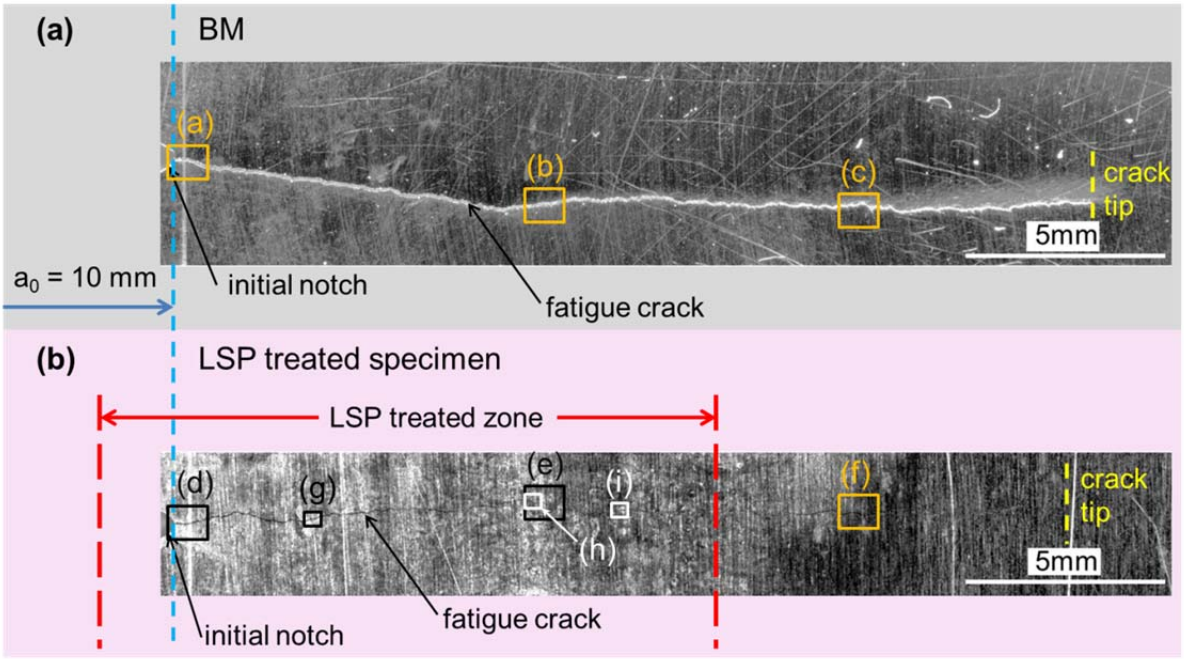

Figure 8. *Macrographs showing the fatigue crack propagation trajectory.*
(a) BM, (b) LSP treated specimen LSP 5x -2.

Optical micrographs of the fatigue crack propagation through the microstructure are shown in Figure 9. Figure 9(a)-(c) show transgranular fracture failure of the AA2024-T351 BM. Close to the notch at a_0 = 10 mm the distance between the fatigue crack flanks is approximately

57 µm (Figure 9(a)) and decreases with increasing crack length. At a crack length of 26.5 µm the distance between the fatigue crack flanks is approximately 15 µm (Figure 9(c)). Moreover, the crack flanks do not show any signs of mechanical contact leading to plastic deformation due to crack closure. In contrast, the LSP treated specimen shows a significantly smaller distance between the fatigue crack flanks of approximately 21 µm close to the initial notch (Figure 9(d)) and the distance is decreased to approximately 15 µm within the middle of the LSP treated zone (Figure 9(e)). At a crack length of a = 26.6 mm the crack flank distance is approximately 18 µm (Figure 9(f)) which is comparable to the crack flank distance of the BM specimen (Figure 9(c)). At higher magnification of regions of crack flank contact, secondary cracks and crack branching are clearly visible (Figure 9(g)-(i)). Such observations were not found in AA2024-T351 BM specimen. Smaller distances between crack flanks, crack flank contacts, secondary cracks as well as crack branching are the result of LSP-induced residual stresses effecting the FCP propagation. The present results obtained from metallographic observation suggest that crack closure is the main cause for appearances of microstructural features when LSP-induced residual stresses are existing.

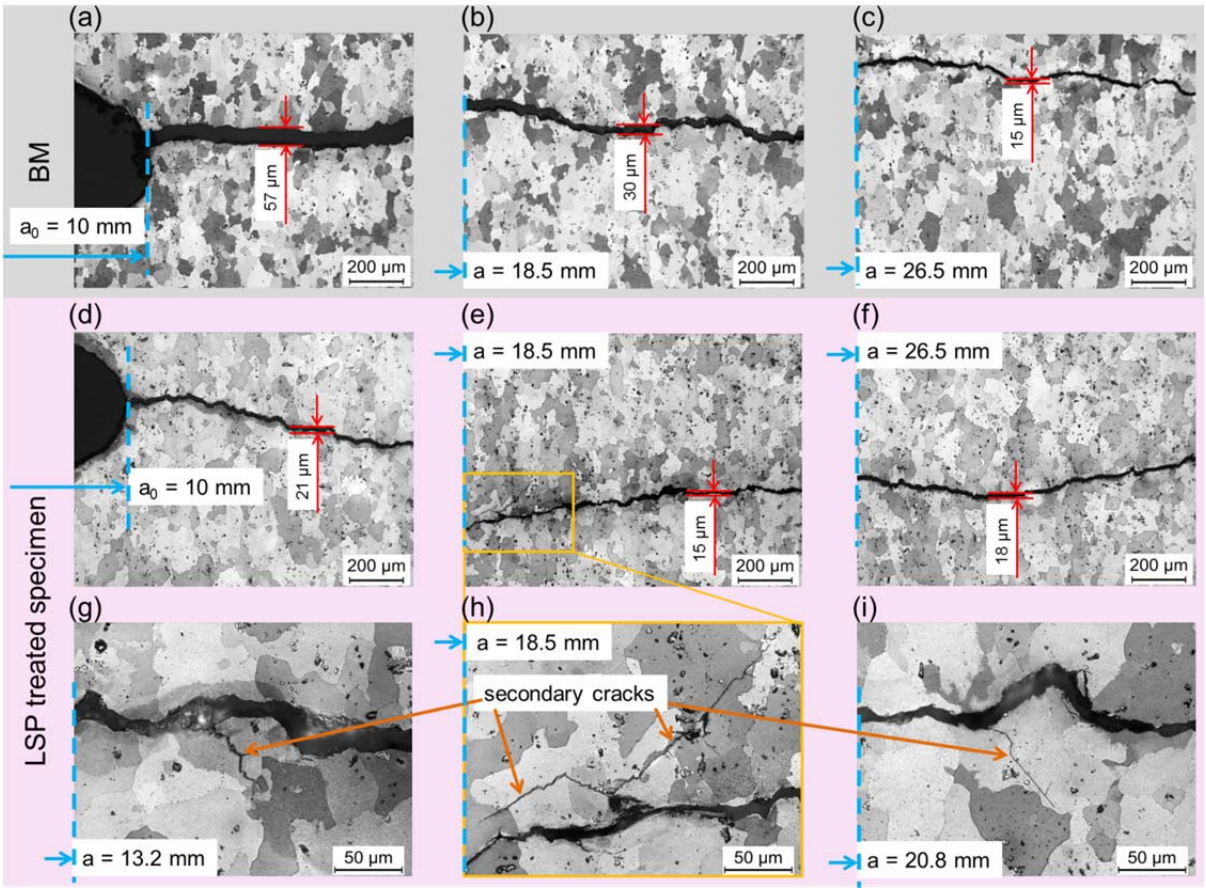

Figure 9. *Optical micrographs of crack growth patterns.*
BM specimen at (a) a_0 = 10 mm, (b) a = 18.5 mm and (c) a = 26.5 mm;
LSP treated specimen LSP 5x -2 at (d) a_0 =10 mm, (e) a = 18.5 mm and (f)at a = 26.5;
Higher magnifications of the LSP treated specimen LSP 5x -2 at
(g) a = 13.2 mm, (h) a = 18.5 mm and (i) a = 20.8 mm.
Positions of the micrographs on fatigue crack trajectories is shown in Figure 8.

A microfractographic analysis was performed to understand the microstructural issues of the FCP in specimens with high residual stresses induced through the LSP treatment. Figure 10 depicts a comparison of the fracture surface for the BM and the specimen with the LSP treatment. The LSP treated specimen exhibits plasticised areas without fatigue striations (Figure 10(b), (d) and (f)) and secondary cracks in the edge regions (Figures 10(b) and (f)). These features were not observed in the BM specimens, where shear lips and fatigue striations are present (Figures 10(a), (c) and (e)). The microfractography results indicate that plasticised areas originated from the close mechanical contact between the crack flanks are supported by the presence of compressive residual stresses.

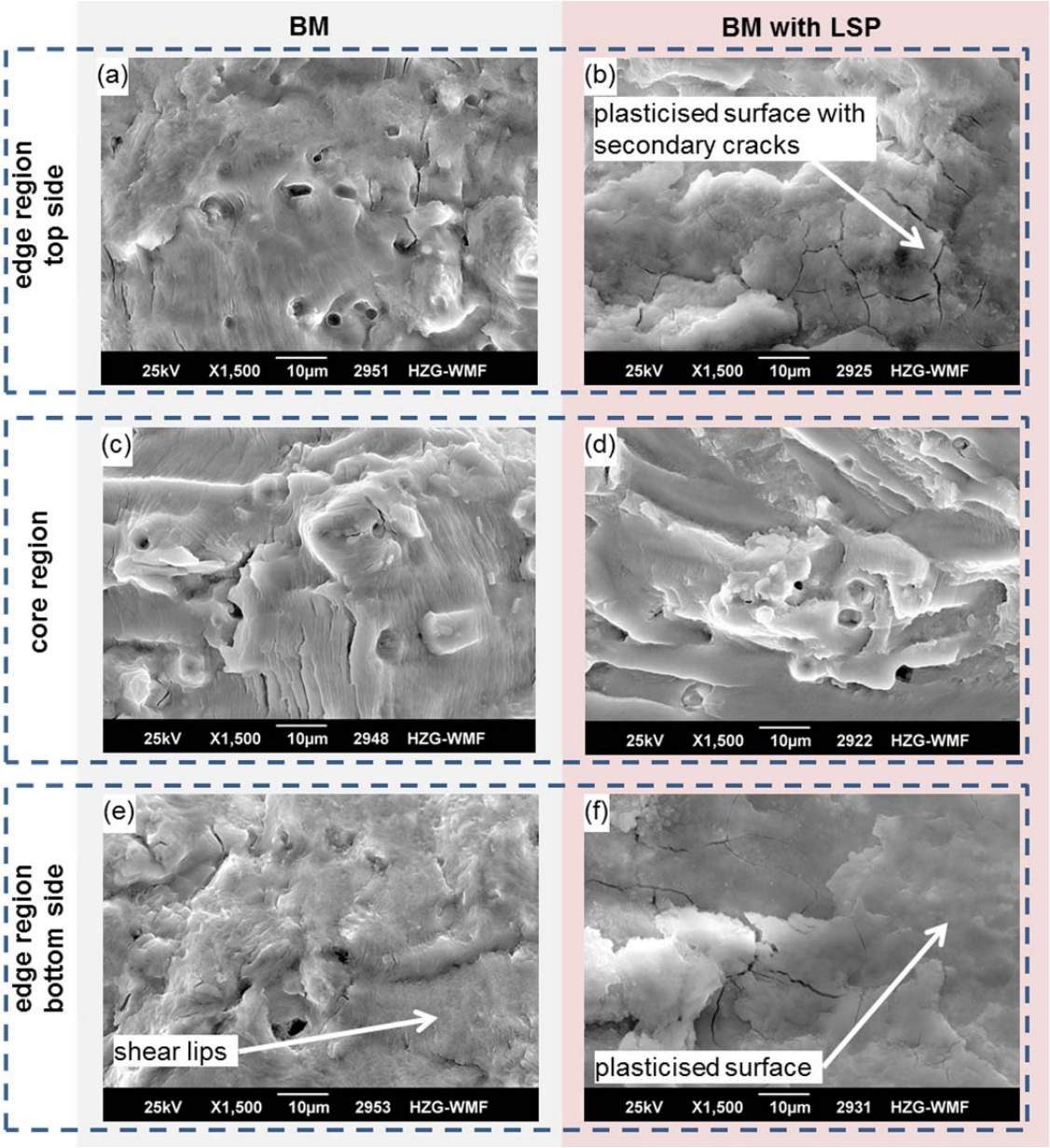

Figure 10. *Overview of the fractured surfaces at a = 20 mm.*
(a), (c) and (e) for the BM specimen; and
(b), (d) and (f) for the LSP treated specimen (LSP 5x -1, Table 1)

4. Consideration of LSP-induced residual stresses in the evaluation of the FCP test results

To understand the retardation of the FCP in the LSP treated specimen, the load vs. the COD curves obtained at different crack lengths were analysed. Throughout the analysed *a/W* region from the beginning of the FCP test (*a/W* = 0.2) to the end of the FCP test (*a/W* = 0.6), the curve for the BM specimen is linear and does not indicate any noticeable inflection points (as can be seen at the beginning of the test, at *a/W* = 0.22 mm, and close to the end of the test, at a/W = 0.56, Figure 11, red curves). In contrast to the BM specimen, the LSP treated specimen depicts inflection points in the load vs. COD curves (blue curves in Figure 11). The curves obtained at different *a/W* values depict different curvatures for the first parts of the curves up to the inflection points. At an *a/W* = 0.22, the curve of the LSP treated specimen indicates a negative curvature (syncline) up to the inflection point at a load value of approximately 0.64 kN (Figure 11(a)). Up to the inflection point, the gradient of the curve is lower than the gradient of the second part of the curve. The gradient of the second part of the curve is comparable to the gradient of the BM curve obtained at the same *a/W* value. The lower gradient of the first part of the curve indicates that tensile residual stresses occur.

For the load vs. COD curve for the LSP treated specimen obtained at the beginning of the test, the ΔCOD indicated the difference between the upper (linear) part of the curve and the first part of the curve through the tensile residual stress located on the right side of the load vs. COD curve (Figure 11(a)). By considering that the ΔCOD before the inflection point (distance between points A and D, Figure 11(a)) resulted from the combination of the effects of the tensile residual stresses, $\Delta COD_{tensile\ RS}$, and the applied load, $\Delta COD_{apl\ load}$, the ΔCOD_{corr} that should contribute to the virtual increase in the applied load due to the presence of tensile stresses as the distance between points C and D can be estimated as $\Delta COD_{apl\ load} - \Delta COD_{tensile\ RS}$ (distance between points A and B is equal to the distance between points B and C). The assumption is that for the ΔCOD before the inflection point, a part from the applied load for ΔCOD_{corr} is not considered in the first part of the curve, i.e., before the inflection point, and therefore has to be added to the end linear part of the curve. The virtual corrected effective maximal load, $F_{max\ eff}$, which considers the effects of the tensile stresses, should include the linear part of the increase to point E to incorporate ΔCOD_{corr} (distance between points C and D is equal to the distance between points C´ and D´). The resulting $F_{max\ eff}$ is approximately 1.4 kN for the load vs. COD curve obtained at an *a/W* value of 0.22, as indicated in Figure 11(a).

The load vs. COD curve obtained at *a/W* = 0.56 initially depicts a positive curvature (anticline). The higher gradient of the first part of the curve indicates that the compressive residual stresses were present and caused the crack closure that influenced the opening load, F_{op}, which increased up to the inflection point of the hysteretic curve. The inflection point of the curve can be considered as the opening load. The ΔCOD indicated the difference between the upper (linear) part of the curve and the first part of the curve through the compressive residual stress located on the left side of the load vs. COD curve. By considering the crack closure effects, the opening load, F_{op}, should be increased to the inflection point of the load vs. COD curve (approximately 0.52 kN, Figure 11(b)).

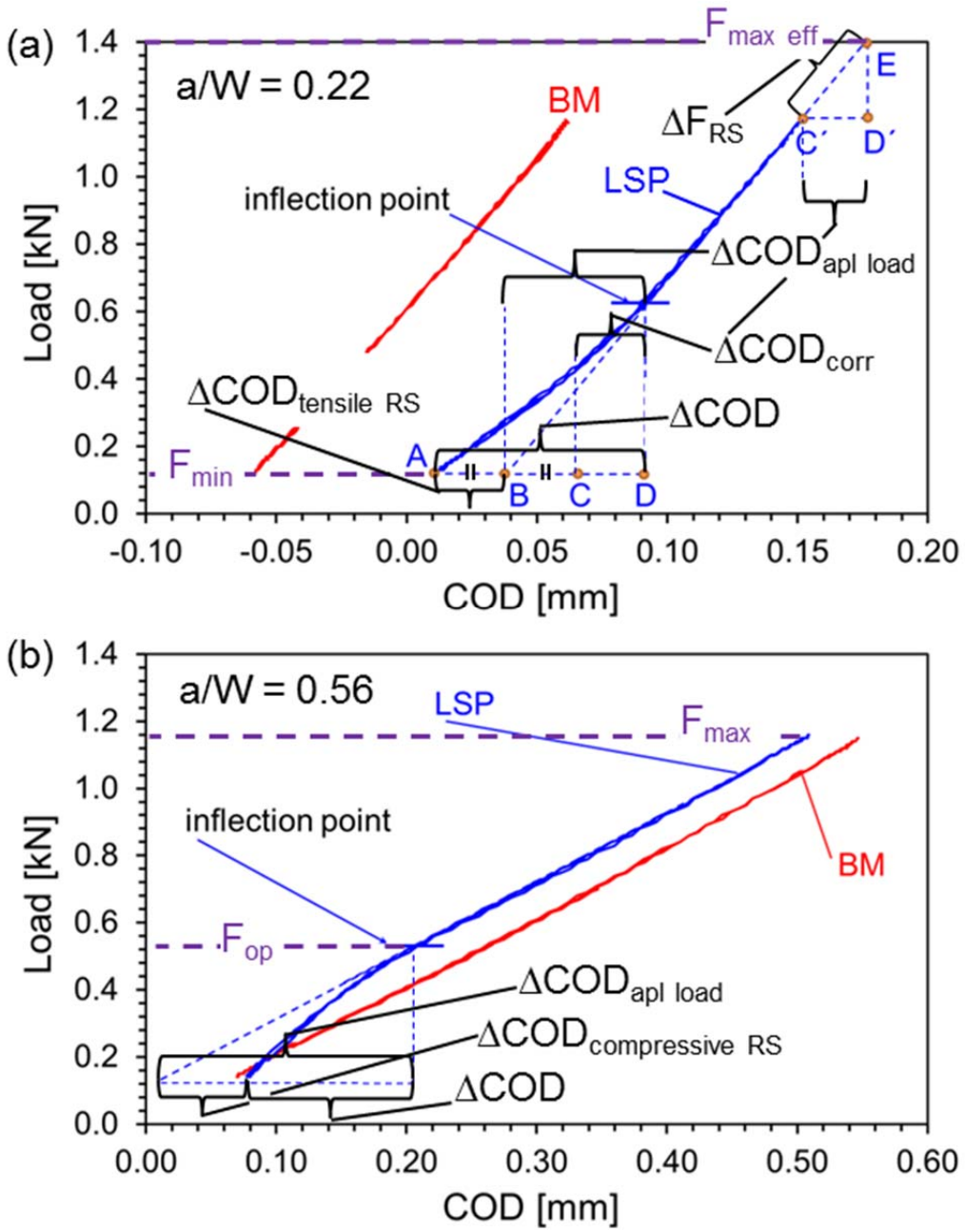

Figure 11. *Load vs. COD curves obtained at different a/W values. (a) BM specimen and LSP treated specimen (LSP 5x -1, Table 1) at the beginning of the FCP test; and (b) BM specimen and LSP treated specimen (LSP 5x -1, Table 1) at an a/W value of 0.56.*

Based on the considerations described above, the load vs. COD curves for the BM specimen and the LSP treated specimens were analysed, and $F_{max\ eff}$ and F_{op} were calculated for the tensile residual stress and compressive residual stress regions, respectively. Then, the effective load ratio, $R_{F\ eff}$, was calculated considering the corrected effective load levels. The effective load ratio values were calculated for the crack length range from a_0 = 10 mm (a/W = 0.2) to a = 30 mm (a/W = 0.6) according to the following equations:

$$R_{F\ eff}(a) = F_{min}(a)/F_{max}(a) \quad (2)$$

for BM specimen,

$$R_{F\ eff}(a) = F_{min}(a)/F_{max\ eff}(a) \quad (3)$$

for LSP treated specimen in tensile residual stress region, and

$R_{F\,eff}(a) = F_{op}(a)/F_{max}(a)$ (4)

for LSP treated specimen in compressive residual stress region, where the $F_{max\ eff}$ and F_{op} are the effective maximum and opening load values, respectively, obtained from the corresponding load vs. COD curves based on considerations described above; F_{min} and F_{max} are the applied load levels during the FCP test.

The calculated effective load ratio values for the specimens tested are presented in Figure 12(a). The crack closure for LSP treated specimens affected the R_F ratio (increased the level of opening load) and therefore reduced the effective load range in the areas with compressive residual stresses. In the tensile residual stress regions, the R_F ratio was insignificantly reduced. The R_F ratio for the BM specimen remained nearly constant during the FCP test. A similar retardation mechanism has been described also for FCP in laser heating induced residual stresses by Schnubel and Huber (2012), with the difference, that there tensile residual stresses are induced in the treated area, surrounded by compressive residual stresses.

Based on the obtained effective maximum and opening load values the so-called effective stress intensity factor range, ΔK_{eff}, values were calculated for the corresponding crack length, a, values in the investigated crack length region according to the following equations:

$\Delta K_{eff}(F, a) = f_K(F_{min}, a)/f_K(F_{max}, a)$ (5)

for BM specimen, $\Delta K = \Delta K_{eff}$,

$\Delta K_{eff}(F, a) = f_K(F_{min}, a)/f_K(F_{max\ eff}, a)$ (6)

for LSP treated specimen in tensile residual stress region, and

$\Delta K_{eff}(F, a) = f_K(F_{op}, a)/f_K(F_{max}, a)$ (7)

for LSP treated specimen in compressive residual stress region, where $f_K(F, a)$ is the function for the calculation of the stress intensity factor (range) according to the Equation (1) in dependence on the corresponding load, F, and the crack length, a.

The FCP rates vs. applied stress intensity factor range, ΔK, are depicted in Figure 12(b). The BM specimens depict a typical linear behaviour in the logarithmic coordinates. The calculated ΔK values for the LSP treated specimens considering the applied load levels F_{min} and F_{max} depict minimum da/dN values at a ΔK value of approximately 20 MPa√m.

By considering the effects of tensile and compressive residual stresses on the effective load range for the calculation of the stress intensity factor range, i.e., the so-called effective stress intensity factor range, ΔK_{eff}, according to the Equations (5)-(7) the da/dN vs. ΔK_{eff} (da/dN values obtained in FCP test, ΔK_{eff} values calculated) curves for the LSP treated specimens are close to the curve of the BM specimen. It is evident that the applied corrections for calculating ΔK_{eff} are reasonable and consider the effects of the tensile/compressive residual stresses induced by the LSP treatment.

The proposed methodology for the calculation of the effective stress intensity factor range values for the LSP treated specimens based on the experimental results of this study can be used for the validation of the FCP prediction methodology which uses the ΔK_{eff} approach. In earlies seventies of the last century Elber (1971) proposed an expression for the FCP rate in

terms of effective stress intensity factor which takes into account the presence of crack opening/crack closure effects. Now it is widely accepted that different da/dN vs. ΔK curves for different stress intensity factor ratios, $R = K_{min}/K_{max}$, can be correlated to a single curve, the so called "master curve", by using the effective stress intensity factor range, ΔK_{eff} (Servetti and Zhang, 2009; Newman Jr., 1984; Schijve, 1981). For the specimen without residual stresses the R ratio is equal to the applied load ratio, R_F. In case of the BM specimen investigated in the current study the crack opening/crack close effects were not observed and therefore the ΔK values calculated taking into account the applied load range are comparable with the ΔK_{eff} values for each crack length value. The basic FCP law in regime II, initially proposed by Paris and Erdogan (1963), can be applied in terms of the effective stress intensity factor range for the prediction of the FCP rate, da/dN:

$$\frac{da}{dN} = C\left(\Delta K_{eff}\right)^{m}, \tag{8}$$

where C and m are material constants, that can be determined experimentally from the FCP test.

For the LSP treated specimen the load vs. COD behaviour can be predicted using FEM taking into account residual stresses and fracture surfaces contact similar to Schnubel et al. (2012). Using the proposed methodology that is described above, the effective stress intensity factor range values can be calculated for each crack length. Using Equation (8) and the calculated ΔK_{eff} values together with experimentally obtained material constants, the da/dN values can be incrementally calculated for each crack length values.

Using the proposed methodology, the da/dN values for the three LSP treated specimens were obtained from the BM curve (master curve in this case) for each ΔK_{eff} value. As each ΔK_{eff} value is correlated to the corresponding crack length, the obtained da/dN values from the "master curve" were represented vs. crack length in Figure 12(c) as "predicted" curves. It is obvious that the three "predicted" curves for the LSP treated specimens are close to the experimentally obtained curves. The validation based on Finite Element results independent from the presented experimental measurements is a further step that should be covered by future work. The crack length as a function of the load cycles $a(N)$ can be easily calculated by integrating the "predicted" da/dN over crack length, a, curves.

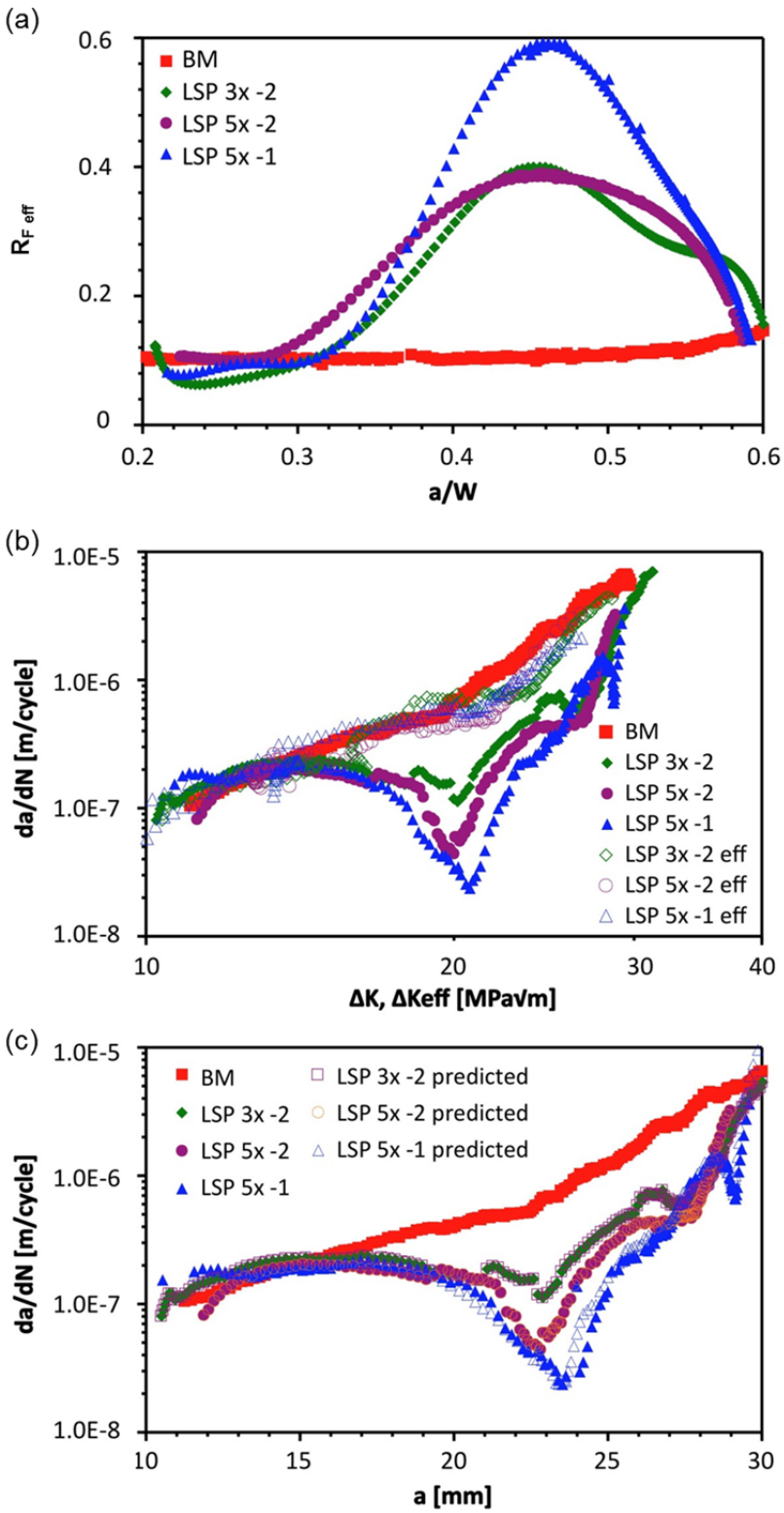

Figure 12. *Correction of effective values under consideration of the LSP-induced residual stresses.*

(a) $R_{F\,eff}$ vs. a/W, (b) da/dN vs. ΔK and ΔKeff and (c) da/dN vs. a.

5. Summary and conclusions

In the presented research, an LSP treatment was performed on C(T) specimens of aluminium alloy AA2024 with a thickness of 2.0 mm using a pulsed high energy Nd:YAG laser. The obtained results indicate that LSP is an effective process for introducing high and deep compressive residual stresses without severe surface damages and deformations in the microstructure of thin AA2024 specimens. LSP is already an established process in aerospace industry for extending the fatigue life of critical thick-section components and the relevant laser and robot technology is commercially available. The results of this study can be similarly transferred to industrial LSP facilities designed for treatment of small-sized components as well as large scale structures.

FCP tests were performed to investigate the retardation effect of LSP residual stresses. Specimens with the LSP treatment reveal a significant retardation of the FCP. Fatigue cracks suffered several crack closures in the region with compressive residual stresses. The presence of crack closure was confirmed through the presence of a frictional contact surface, thus leading to a smoothened surface topography. This effect was not observed in the BM, where shear fracture, fatigue striations, fatigue lines and fracture paths were clearly visible. Furthermore, the additional contribution of residual stress to the closure level was seen in the load vs. crack opening displacement curves. The presence of compressive residual stresses caused the crack closure effect, which increased the level of opening load and therefore reduced the effective load range.

An original methodology on how to consider LSP-induced residual stresses on the FCP behaviour was proposed. It was shown, that the effective stress intensity factor range can be calculated based on the experimentally obtained load vs. crack opening displacement curves. The load vs. crack opening displacement curves can be predicted for the LSP treated specimen using FEM taking into account residual stresses and contact of fractured surfaces. Therefore, it should be possible to calculate effective stress intensity factor and predict the fatigue crack propagation using the basic FCP law in terms of the effective stress intensity factor.

Based on the obtained results and taking into account industrial LSP facilities the technology can be considered as a potential tool for the surface treatment of aluminium alloy airframe structures. Two possible application scenarios, where LSP can also be applied on thin structures, could be considered: design and repair. If the retardation effect of LSP-induced residual stresses can be predicted for a structural component, aircraft structures can be designed accounting for the LSP-induced residual stresses to improve the damage tolerance behaviour. The significant retardation effect of LSP on FCP behaviour can be used for repair of structural components, where small cracks are detected. Here, LSP treatment can be used to arrest cracks and decelerate the FCP.

Acknowledgements

We acknowledge Deutsches Elektronen-Synchroton (DESY), Germany for using synchrotron radiation diffraction at the beamline P07B, which is operated by the German Engineering Materials Science Centre (GEMS) of the Helmholtz-Zentrum Geesthacht. The authors would also like to thank the following project members for their valuable work and support: H. Tek

(mechanical testing), L. Moura (using the hole drilling system) and F. Dorn (specimen preparation). The authors especially thank the former colleague Dr. W. V. Vaidya (now retired) for his valuable comments.

References

Bergant, Z., Trdan, U., Grum, J. (2016), "Effects of laser shock processing on high cycle fatigue crack growth rate and fracture toughness of aluminium alloy 6082-T651", *International Journal of Fatigue*, Vol. 87, pp. 444-455.

Chupakhin, S., Kashaev, N., Huber, N. (2016), "Effect of elasto-plastic material behaviour on determination of residual stress profiles using the hole drilling method", *The Journal of Strain Analysis for Engineering Design*, Vol. 51 No. 8, pp. 572-581.

Elber, W. (1971), "The significance of fatigue crack closure", *ASTM Special Technical Publication 486*, pp. 230-242.

Enz, J., Khomenko, V., Riekehr, S., Ventzke, V., Huber, N., Kashaev, N. (2015), "Single-sided laser beam welding of a dissimilar AA2024–AA7050 T-joint", *Materials and Design*, Vol. 76, pp. 110-116.

Gariépy, A., Bridier, F., Hoseini, M., Bocher, P., Perron, C., Lévesque, M. (2013), "Experimental and numerical investigation of material heterogeneity in shot peened aluminium alloy AA2024-T351", *Surface and Coatings Technology*, Vol. 219, pp. 15-30.

Hammersley, A.P., Svensson, S.O., Hanfland, M., Fitch, A.N., Häusermann, D. (1996), "Two-dimensional detector software: From real detector to idealised image or two-theta scan", *High Pressure Research*, Vol. 14, pp. 235-248.

Hatamleh, O., Lyons, J. and Forman, R. (2007), "Laser and shot peening effects on fatigue crack growth in friction stir welded 7075-T7351 aluminium alloy joints", *International Journal of Fatigue*, Vol. 29 No. 3, pp. 421–434.

Hatamleh, O. (2009), "A comprehensive investigation on the effects of laser and shot peening on fatigue crack growth in friction stir welded AA2195 joint", *International Journal of Fatigue*, Vol. 31 No. 5, pp. 974–988.

Hombergsmeier, E., Holzinger, V., Heckenberger, U.C. (2014), "Fatigue crack retardation in LSP and SP treated aluminium specimens", *Advanced Materials Research*, Vol. 891-892, pp. 986-991.

Huber, N. and Heerens, J. (2008), "On the effect of a general residual stress state on indentation and hardness testing", *Acta Materialia*, Vol. 56, pp. 6205–6213.

Lodini, A., Fitzpatrick, M.E. (Eds.), (2003), *Analysis of residual stress by diffraction using neutron and synchrotron radiation*, Taylor & Francis, London.

Lados, D.A. and Apelian, D. (2006), "The effect of residual stress on the fatigue crack growth behaviour of Al-Si-Mg cast alloys – Mechanisms and corrective mathematical models", *Metallurgical and Materials Transactions A*, Vol. 37A, pp. 133-145.

Newman Jr., J.C. (1984), "A crack opening stress equation for fatigue crack growth", *International Journal of Fracture*, Vol. 24, pp. 131-135.

Paris, P.C. and Erdogan, F. (1963), "A critical analysis of crack propagation laws", *Journal of Basic Engineering*, Vol. 85, pp. 528-534.

Rouleau, B., Peyre, P., Breuils, J., Pelletier, H., Baudin, T., Brisset, F. (2011), "Characterization at a local scale of a laser-shock peened aluminium alloy surface", *Applied Surface Science*, Vol. 257, pp. 7195-7203.

Schijve, J. (1981), "Some formulas for the crack opening stress level", *Engineering Fracture Mechanics*, Vol. 14 No. 3, pp. 461-465.

Schnubel, D. and Huber, N. (2012), "The influence of crack face contact on the prediction of fatigue crack propagation in residual stress fields", *Engineering Fracture Mechanics*, Vol. 84, pp. 15-24.

Servetti, G., Zhang, X. (2009), "Prediction fatigue crack growth rate in a welded butt joint: The role of effective *R* ratio in accounting for residual stress effect", *Engineering Fracture Mechanics*, Vol. 76, pp. 1589-1602.

Steinzig, M. and Ponslet, E. (2003), "Residual stress measurement using the hole drilling method and laser speckle interferometry: Part 1", *Experimental Techniques*, Vol. 27 Issue 3, pp. 43-46.

Tan, Y., Wu, G., Yang, J.M., and Pan, T. (2004), "LSP on fatigue crack growth behaviour of aluminium alloy", *Fatigue & Fracture of Engineering Materials & Structures*, Vol. 27 No. 8, pp. 649–656.